S©MR

СИБИРСКИЕ ЭЛЕКТРОННЫЕ
МАТЕМАТИЧЕСКИЕ ИЗВЕСТИЯ
Siberian Electronic Mathematical Reports
http://semr.math.nsc.ru
ISSN 1813-3304

Vol. 23, No. 1, pp. 321–342 (2026)
https://doi.org/10.33048/semi.2026.23.020

УДК 539.3
MSC 74F10

THERMOPOROELASTIC STRENGTH ANALYSIS OF PRE-STRESSED CASED AND CEMENTED WELL

K.S. SUKHININA, **A.V. VALOV**, AND **A.V. SHUTOV**

Communicated by M.I. Protasov

Abstract: Well integrity depends on the mechanical stability of the casing-cement-formation system under thermo-mechanical loads induced by variations in temperature, pore pressure, and *in-situ* stresses. This study develops a numerical model for evaluating stress evolution in pre-stressed cased and cemented wells using a thermoporoelastic formulation. Two limiting loading conditions are examined: a newly created well, where the initial stress state is primarily governed by the cementing stage and volumetric shrinkage; and a late-life stage of the well's lifecycle, where both the cement sheath and the surrounding formation undergo dominant creep. The model accounts for poroelastic material behavior, thermal stresses, *in-situ* stress anisotropy, and casing eccentricity. To verify the implemented numerical algorithm, a closed-form analytical solution for the steady-state creep of an incompressible viscous medium around a circular cavity has been derived. Numerical simulations identify potential failure zones using the Drucker-Prager criterion. The results show that stresses established in the

Sukhinina K.S., Valov A.V., Shutov A.V., Thermoporoelastic strength analysis of pre-stressed cased and cemented well.

The research was carried out with the financial support of the Russian Federation represented by the Ministry of Science and Higher Education through grant № 075-15-2023-588.

Received December, 6, 2025, Published April, 17, 2026.

early stage are substantially reduced during creep-driven relaxation. In the case of long-term creep, the size of the potential failure zones decreases, reducing the risk of interfacial debonding or cracking. By explicitly incorporating the multi-stage construction history to define the initial stress state, the framework highlights the critical importance of a consistent initial-state formulation.

Keywords: thermoporoelasticity, well integrity, cased and cemented well, multi-stage loading

1 Introduction

Maintaining the integrity of cased and cemented wells is a fundamental requirement for the safe operation of oil and gas wells as underground facilities. Loss of cement sheath mechanical stability can result in fluid leakage and the formation of high-risk zones [1, 2]. The importance of such analyses is further amplified in the context of contemporary engineering operations, including hydraulic fracturing, enhanced oil recovery methods, and CO_2 injection for geological storage. The casing and cement sheath play a critical role in ensuring zonal isolation and preventing cross-formational fluid migration [25].

Extensive research has focused on modeling the mechanical behavior of cementitious materials and surrounding formations [4, 5]. Thermoporoelastic formulations enable the analysis of stress and strain distributions in the near-wellbore region under variable pressure and temperature conditions. Although more advanced models include plasticity and damage evolution, linear elastic and thermoporoelastic formulations remain common because they are computationally efficient and still capture the key physics of the casing–cement–rock system [6].

The key component of well integrity analysis is the use of a multi-stage modeling framework. The stress state established during drilling and cementing defines the initial conditions that determine the subsequent mechanical behavior of the system [7, 8]. Operational loads are applied to this initial state and lead to additional stress redistribution. This approach enables consistent representation of both newly created and late-life wells.

Immediately after placement, the cement sheath is prone to hydration-induced shrinkage, which can create micro-annuli along the casing-cement and cement-rock interfaces. Over longer timescales, the creep behavior of both the cement and the formation becomes increasingly important. Experimental studies show that cement undergoes stress relaxation and progressive strain accumulation, particularly under combined thermal and moisture conditions [9, 10]. Formations, including shales, also exhibit creep even in dry environments, and this time-dependent deformation can markedly modify the stress state over relatively short periods [11]. These processes act to

redistribute and partially equilibrate stresses between the cement and the formation while maintaining the *in-situ* stress contrast.

Thermal gradients and cyclic loading during well operations generate substantial stresses. These stresses arise from processes such as cooling during CO_2 injection or temperature variations during operational cycles. Thermal cycling is known to induce repeated casing expansion and contraction, potentially leading to debonding at the casing-cement and cement-formation interfaces. This process facilitates the creation of micro-annuli and crack development within the cement sheath, ultimately compromising its sealing capacity and increasing the risk of leakage [12, 5]. Critical parameters controlling these effects are the magnitude of the temperature change, the rate of thermal loading, and the duration of the thermal cycles [13]. Furthermore, thermomechanical coupling, such as from pre-injection cooling, significantly alters stability predictions and failure criteria. This underscores the necessity of incorporating thermal effects even in simplified models [14, 15].

In this study, we develop a thermoporoelastic model in which the mechanical and pore-pressure fields are fully coupled, while the thermal field is treated within a semi-coupled manner. The coupled and decoupled formulations yield similar results under simplifying assumptions [16]. This provides a useful basis for adopting the semi-coupled approach without significant loss of accuracy. We examine two representative scenarios. The first reflects a newly created well in which the initial stress state is primarily governed by the cementing stage and volumetric shrinkage. The second corresponds to a late-life well in which both the cement sheath and the surrounding formation undergo dominant creep. In the long-term creep scenario, the formation and cement behave like an incompressible viscous fluid. Comparing these scenarios illustrates how initial stress conditions and time-dependent relaxation processes influence long-term wellbore stability. We also investigate the effect of casing eccentricity on stress distribution in the near-wellbore region.

2 Formulation of the wellbore loading problem

This paper considers the deformation of a cased and cemented well during fluid injection. Figure 1 shows a schematic of the well construction. The casing string is installed during drilling to stabilize the borehole and ensure isolation between different geological layers. At the next stage, the annular space between the casing and borehole is filled with cement slurry. The primary objective of cementing is to create a reliable protective barrier around the wellbore that prevents the vertical migration of reservoir fluids and gases, as well as the contamination of aquifers. Cementing ensures long-term wellbore stability and safety operation, which are crucial in hydrocarbon production.

A right-handed Cartesian coordinate system is introduced, where the z-axis points vertically along the wellbore axis, while the x- and y-axes lie in the horizontal cross-sectional plane (Figure 2). The axes x and y are aligned

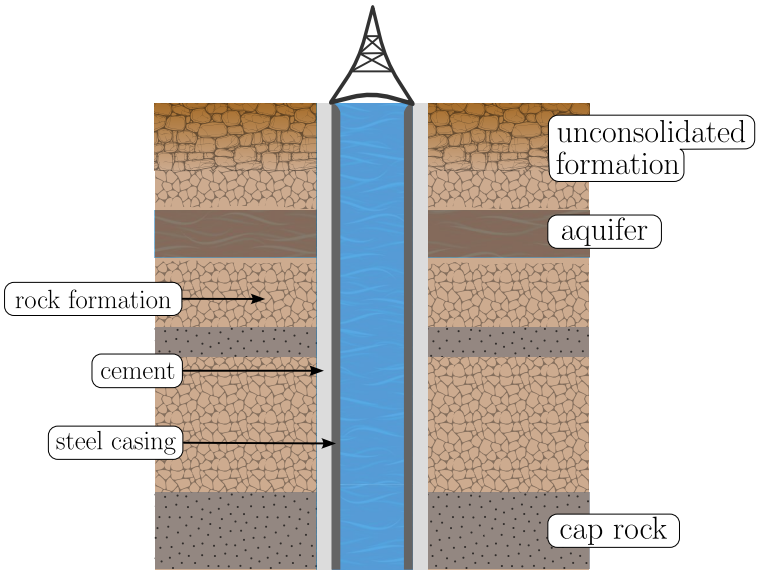

FIG. 1. Schematic representation of a cased and cemented wellbore.

with the directions of the minimum $\sigma_{\min}$ and maximum $\sigma_{\max}$ horizontal *in-situ* stresses, respectively. The *plane strain* approximation is employed, and the small strain theory is applied [6]. The vertical component of displacement is zero: $\mathbf{u} = (u_x, u_y, 0)$. The displacement, pore pressure, and temperature fields are assumed to be independent of z. For simplicity, all vectors, tensors, and differential operators are treated as two-dimensional unless otherwise specified.

The computational domain represents an annular region $V \subset \mathbb{R}^2$ (Fig. 2, left). It consists of a multilayer composite structure: a steel casing (inner layer), a cement sheath (intermediate layer), and the formation (outer layer). The casing can be offset from the axis of the well during placement. To mitigate this effect, centralizers are used to control the casing concentricity within the borehole. In practice, however, insufficient centralization during installation may still lead to a significant offset. Referring to the right panel of Figure 2, the model incorporates casing eccentricity, characterized by the offset δ between the casing and wellbore axes, as well as the orientation angle γ.

The domain boundaries are defined as follows: Γ_∞ denotes the external boundary of the formation, Γ_{SC} is the casing-cement interface, Γ_{CF} represents the cement-formation interface, and Γ_{in} is the inner boundary of the casing.

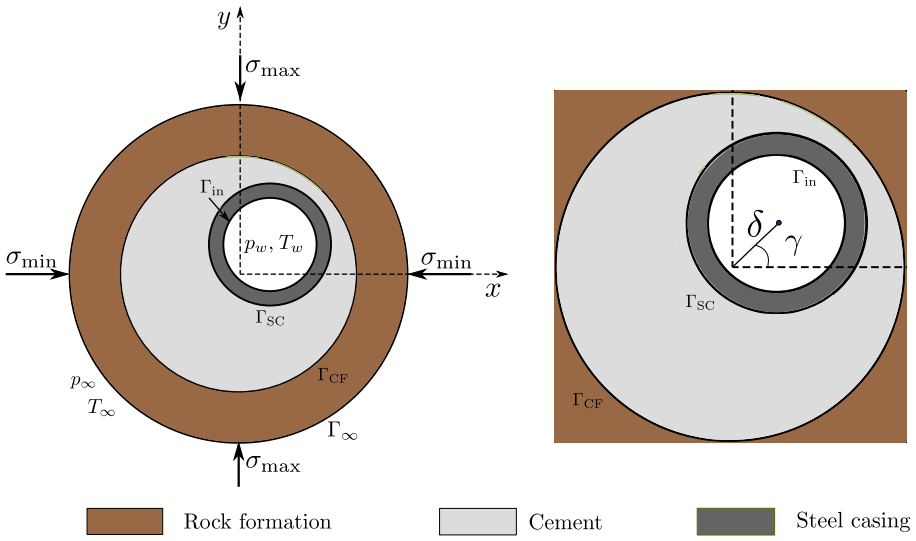

FIG. 2. Cross-sectional view of the wellbore. Brown represents the rock formation, light grey is the cement sheath, and grey is the steel casing.

3 Multi-stage wellbore loading

The integrity of a well fundamentally depends on the stability of its geological and engineered barriers in ensuring zonal isolation over time. To model the system's evolution, this study adopts a two-regime constitutive framework that captures the limitations of its thermomechanical behavior.

The first regime represents the early life of a well, where the stress state is primarily governed by initial cement placement, volumetric shrinkage and subsequent thermoelastic loading, with negligible influence from time-dependent creep. The second regime corresponds to a late-life stage of the well, where long-term creep relaxation has progressively redistributed stresses, leading the system toward a viscous equilibrium state. The analysis of the two limiting cases provides two bounding solutions for well response. It is expected that real-life field-scale conditions are between these two limiting cases [3].

3.1. Early-time regime. Multi-stage modeling provides a systematic framework for describing the loading history of a composite wellbore system [17, 18]. This approach accounts for the mechanical effects that arise during drilling, casing installation, and cementing, which define the initial stress state of the cement sheath and strongly influence its long-term integrity.

To illustrate this, we consider a typical loading sequence during the early stages of the well lifecycle. The initial stress state is controlled by *in-situ* geomechanical conditions and by stresses induced during cementing, while

creep effects are neglected. The sequence consists of three consecutive stages (Figure 3).

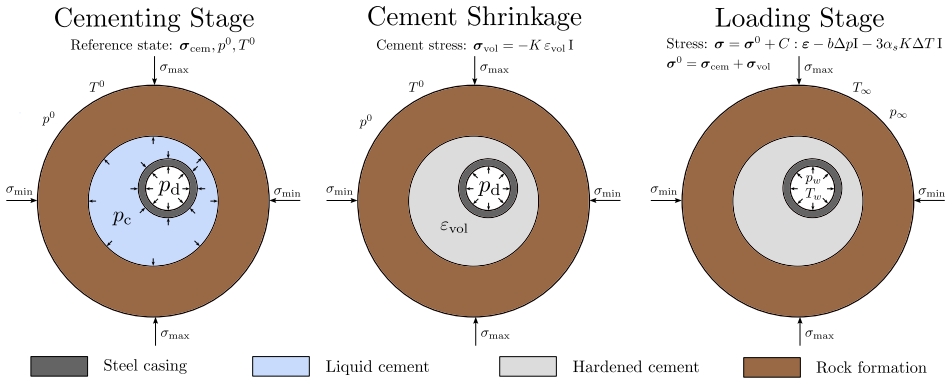

FIG. 3. Schematic representation of the loading scheme applied to the wellbore during the early stages of its lifecycle, including cementing, cement shrinkage, and subsequent operational loading.

Cementing stage. After drilling, a steel casing is inserted into the borehole, and the annulus between the casing and the formation is filled with cement slurry. The liquid cement exerts a hydrostatic pressure p_{c} on the casing and the formation wall, while the inner casing wall is subjected to the displacement fluid pressure p_{d} (Fig. 3, left). The stress field in the casing is described by the Lamé solution [32] for a hollow cylinder loaded by p_{d} and p_{c}, whereas the cement is in hydrostatic equilibrium

$$\sigma^c_{rr} = \sigma^c_{\theta\theta} = -p_{\text{c}}. \tag{1}$$

The surrounding rock is modeled by the Kirsch solution [20, 19], representing a cavity under anisotropic far-field stresses $\sigma_{\min}$ and $\sigma_{\max}$ with internal pressure p_{c}.

Cement volumetric shrinkage. As the cement sets and loses mobility, it undergoes chemical shrinkage that can no longer be compensated for by fluid flow (Fig. 3, middle). This results in an isotropic compressive stress in the sheath, represented as

$$\boldsymbol{\sigma}_{\text{vol}} = -K\varepsilon_{\text{vol}}\mathbf{I}, \tag{2}$$

where K is the bulk modulus of cement and ε_{vol} is the volumetric shrinkage strain, defined such that positive values correspond to shrinkage. Downhole measurements indicate typical values of $\varepsilon_{\text{vol}} \approx 0.001$–$0.004$ (0.1–0.4%) [21, 22, 23, 24].

Operational loading stage. During operation, the well is subjected to the injection of a fluid (e.g., supercritical CO_2) at a pressure p_w and temperature T_w (Fig. 3, right). At this stage, the cement sheath is not in direct contact with the injected fluid due to the impermeable casing, but it experiences stress redistribution due to the applied load.

The initial stress state is determined as the superposition of the stresses arising from the cementing process and those resulting from volumetric shrinkage:

$$\boldsymbol{\sigma}^0 = \boldsymbol{\sigma}_{\text{cem}} + \boldsymbol{\sigma}_{\text{vol}}. \tag{3}$$

The vertical component of the initial stress tensor, σ^0_{zz}, is evaluated differently for each material: for the casing according to plane strain conditions $\sigma^0_{zz} = \nu(\sigma_{xx} + \sigma_{yy})$; hydrostatic stress for the cement sheath $\sigma^0_{zz} = p_{\text{c}}$; and for the formation $\sigma^0_{zz} = -\sigma_v + \nu\left[(\sigma_{xx} - \sigma_{\min}) + (\sigma_{yy} - \sigma_{\max})\right]$, where σ_v represents the vertical geological stress, ν is Poisson's ratio, and σ_{xx} and σ_{yy} denote the horizontal stress components. This formulation captures the stress redistribution induced by elastic interactions within the system.

We adopt a linear thermoporoelastic model with material properties for steel, cement, and rock. The poromechanical part of the problem is treated in a fully coupled manner, while the thermal field is incorporated in a semi-coupled way: temperature is obtained from the heat equation and subsequently enters the poromechanical formulation through thermal strains. Body forces, internal heat sources, and convection on the external boundary are neglected. The internal interfaces between the casing and cement, and between the cement and formation, are assumed to be perfectly bonded.

The equilibrium equation expresses the balance of linear momentum, and the constitutive law for each material subdomain is given by

$$\operatorname{div}\boldsymbol{\sigma} = 0, \quad \boldsymbol{\sigma} = \boldsymbol{\sigma}^0 + \mathbb{C} : \boldsymbol{\varepsilon} - b(p - p^0)\mathbf{I} - 3\alpha_s K(T - T^0)\mathbf{I}, \tag{4}$$

where $\boldsymbol{\sigma}$ is the Cauchy stress tensor, $\boldsymbol{\sigma}^0$ is the initial stress tensor (scenario-dependent), $\boldsymbol{\varepsilon}$ is the strain tensor with respect to the reference state before operational loading, b is Biot's coefficient, p is the pore pressure, p^0 is the reference pore pressure, α_s is the skeleton linear thermal expansion coefficient, $K = (3\lambda + 2G)/3$ is the bulk modulus of the material, with G and λ being the Lamé parameters, T is the temperature, and T^0 is the reference temperature. The fourth-order elasticity tensor is

$$\mathbb{C} : \boldsymbol{\varepsilon} = \lambda \operatorname{tr}(\boldsymbol{\varepsilon})\,\mathbf{I} + 2G\,\boldsymbol{\varepsilon}. \tag{5}$$

By substituting Darcy's law into the mass conservation equation and applying the thermomechanical relations [6], the governing equation for pore pressure is obtained

$$b\,\frac{\partial(\operatorname{tr}\boldsymbol{\varepsilon})}{\partial t} + \frac{1}{M}\frac{\partial p}{\partial t} - \operatorname{div}\left(\frac{k}{\mu_f}\nabla(p)\right) = 3\alpha_m \frac{\partial T}{\partial t}, \tag{6}$$

where k is the permeability and μ_f is the pore fluid viscosity. The parameter M denotes Biot's modulus for the saturated medium, defined by the relation $1/M = (b - \phi^0)(1 - b)/K + \phi^0/K_f$, where K_f is the bulk modulus of the pore fluid and ϕ^0 is the initial porosity. The volumetric thermal expansion coefficient for the saturated material α_m is given by $\alpha_m = (b - \phi^0)\alpha_s + \phi^0\alpha_f$, which incorporates the thermal expansion coefficients of the solid skeleton α_s and the pore fluid α_f.

In the absence of internal sources, the transient heat conduction equation governs the evolution of the temperature field in the considered domain as follows

$$C_m \frac{\partial T}{\partial t} - \operatorname{div}(\kappa \nabla(T)) = 0, \tag{7}$$

where κ is the thermal conductivity, $C_m = (1-\phi^0)\rho_s C_s + \phi^0 \rho_f C_f$ is the material volumetric heat capacity, and C_s and C_f are the specific heat capacities of the solid and fluid, respectively

At the inner boundary Γ_{in} (Figure 2), the pressure of the fluid in the wellbore $p_w(t)$ is prescribed, along with the prescribed temperature $T_w(t)$

$$\Gamma_{\text{in}} : \boldsymbol{\sigma} \cdot \mathbf{n} = -p_w(t)\mathbf{n}, \quad T = T_w(t), \tag{8}$$

where $\mathbf{n}$ denotes the outward unit normal vector to the boundary.

At the internal interfaces, a perfect bond is assumed, which ensures mechanical continuity at the interface. This ensures mechanical continuity at the interfaces by enforcing the continuity of displacements and normal stresses. In addition, the continuity of pore pressure and fluid flux is enforced at porous interfaces, and the continuity of temperature and heat flux is imposed across all interfaces. On the steel–cement interface, a no-flux condition is applied for the pore pressure, while in the steel region only thermoelastic equations are solved, since steel is non-porous.

The external boundary conditions represent the influence of *in-situ* stress, formation pore pressure, and formation temperature

$$\Gamma_{\infty} : \boldsymbol{\sigma} \cdot \mathbf{n} = -\operatorname{diag}(\sigma_{\min}, \sigma_{\max}) \cdot \mathbf{n}, \quad p = p_{\infty}, \quad T = T_{\infty}. \tag{9}$$

Here, $\operatorname{diag}(\sigma_{\min}, \sigma_{\max})$ denotes a 2×2 diagonal matrix with diagonal entries $\sigma_{\min}, \sigma_{\max}$.

The initial conditions for the operational stage are

$$t = 0 : \quad \mathbf{u} = \mathbf{0}, \quad \boldsymbol{\sigma} = \boldsymbol{\sigma}^0, \quad p = p^0, \quad T = T^0, \tag{10}$$

where p^0 and T^0 denote reservoir pore pressure and temperature at the considered depth. It should be emphasized that the pressure of the mud and slurry, as well as the shrinkage strain, define the initial stress state through boundary conditions. They do not generate additional loads in the subsequent operational stage.

3.2. Long-term regime. Over time, after drilling and cementing, the stress-strain state of the wellbore system undergoes a significant evolution. In the early stages, cement shrinkage and initial casing loading dominate the behavior, whereas in the long-term regime, creep becomes the primary factor. Under prolonged exposure to *in-situ* stresses and reservoir temperatures, elastic strains become negligible, and the material enters the steady-state creep regime. In this case, the initial stress field is governed not by elastic effects but by the long-term adaptation of the formation-cement-casing system to the applied loads.

The resulting stress analysis for a long-term wellbore response is divided into two stages (Figure 4).

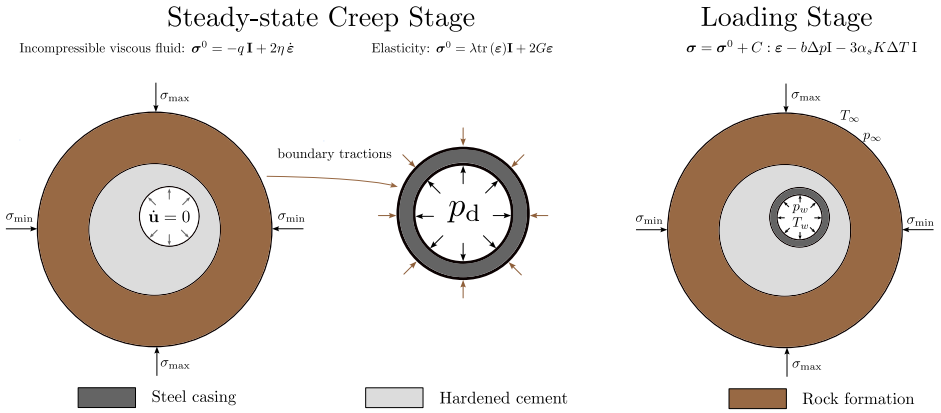

FIG. 4. Loading scheme for a long-term wellbore regime, including a steady-state creep stage followed by operational loading stage

Steady-state creep stage. In problems describing the long-term behavior of materials, the transition to steady-state creep is of primary importance. At sufficiently long loading times, elastic strains become negligible compared to creep strains, and the system approaches a stationary state. In this regime, the distributions of stresses and strain rates depend only on spatial coordinates while remaining constant over time.

The mathematical formulation of the steady-state creep problem includes equilibrium equations and compatibility conditions for strain rates

$$\operatorname{div} \boldsymbol{\sigma}^0 = 0, \qquad \dot{\boldsymbol{\varepsilon}} = \operatorname{sym}(\nabla \dot{\mathbf{u}}), \tag{11}$$

where $\boldsymbol{\sigma}^0$ is the stress tensor associated with the steady-state creep solution, $\dot{\boldsymbol{\varepsilon}}$ is the strain-rate tensor, and $\dot{\mathbf{u}}$ is the velocity vector. For a viscous incompressible medium, the Newtonian fluid model is adopted:

$$(\boldsymbol{\sigma}^0)^D = 2\eta \dot{\boldsymbol{\varepsilon}}^D, \qquad \mathrm{tr}\,(\dot{\boldsymbol{\varepsilon}}) = 0, \tag{12}$$

where η is the viscosity, and the superscript D denotes the deviatoric part of a tensor.

Thus, the problem of determining the steady-state stress distribution under creep can be reformulated as an auxiliary problem of incompressible viscous fluid in the small-strain regime [26], where the stress tensor is decomposed as

$$\boldsymbol{\sigma}^0 = -q\,\mathbf{I} + 2\eta\,\dot{\boldsymbol{\varepsilon}}, \tag{13}$$

and the scalar field q is the mean hydrostatic stress which acts as the Lagrange multiplier and enforces the incompressibility constraint (12). This auxiliary formulation provides a consistent and efficient way to describe the steady-state creep behavior of materials.

On the time scales considered and under the typical loads and temperatures considered in this study, the steel casing is assumed to remain purely elastic and unaffected by creep, which implies $\dot{\boldsymbol{\varepsilon}} = 0$. In the auxiliary formulation for creeping phases, the inner boundary of the cement sheath is constrained by a homogeneous Dirichlet condition $\dot{\mathbf{u}} = 0$. The external boundary conditions for creeping phases account for the effects of the *in-situ* stress field, representing the far-field confinement acting on the outer surface of the rock domain $\boldsymbol{\sigma} \cdot \mathbf{n} = -\mathrm{diag}(\sigma_{\min}, \sigma_{\max}) \cdot \mathbf{n}$. The stresses obtained at the cement-steel interface are then transferred as boundary conditions to the elastic subproblem for the casing (Figure 4). This subproblem reduces to the classical Lamé solution with internal pressure p_d and external loading imposed by the surrounding formation-cement system.

In summary, the computation of the initial stress state under the steady-state creep assumption proceeds in two stages. First, the auxiliary viscous problem for an incompressible medium is solved to obtain the stress distribution in rock and cement. These stresses are then used as boundary conditions for the elastic problem in the casing, where the stress distribution in the steel is determined. This approach provides a consistent representation of phase interaction and yields a physically justified initial stress field for the system. Operational loading stage. The well is subsequently subjected to injection conditions characterized by the pressure p_w and temperature T_w. During this stage, the far-field anisotropy $(\sigma_{\max}, \sigma_{\min})$ governs the stress redistribution around the well, while the initial state is obtained after steady-state creep.

In the limiting creep scenario, which is always preceded by a no-creep stage, the vertical component of the initial stress tensor σ^0_{zz} is specified individually for each subdomain. For the casing, it is computed as

$$\sigma^0_{zz} = \nu(\sigma_{xx} + \sigma_{yy}), \tag{14}$$

where ν is Poisson's ratio and σ_{xx}, σ_{yy} are the horizontal stress components. For the cement sheath, the stress accounts for both the initial hydrostatic pressure and elastic interactions:

$$\sigma^0_{zz} = -p_{\mathrm{c}} + \nu\left[(\sigma_{xx} - p_{\mathrm{c}}) + (\sigma_{yy} - p_{\mathrm{c}})\right], \tag{15}$$

where p_{c} is the hydrostatic stress exerted at the no-creep stage in the cement sheath. Finally, for the formation, the vertical stress incorporates the far-field geological stresses and the elastic redistribution:

$$\sigma^0_{zz} = -\sigma_v + \nu\left[(\sigma_{xx} - \sigma_{\min}) + (\sigma_{yy} - \sigma_{\max})\right], \tag{16}$$

where σ_v denotes the vertical geological stress, and $\sigma_{\min}$ and $\sigma_{\max}$ are the minimum and maximum horizontal stresses, respectively. This formulation ensures that the vertical component of the stress tensor reflects both the prior loading history and the elastic interactions within each subdomain during the limiting creep regime.

The mathematical formulation of this regime remains identical to that described in Section 3, but with the initial stress state defined through the steady-state creep assumption.

4 Numerical implementation

The numerical procedure consists of several consecutive stages that correspond to different physical regimes of the wellbore system. These stages are designed to study how different initial states influence the subsequent loading response. Numerical simulations were conducted using home-made research code based on the `deal.II` library [31].

Initial stress problem. At the early stage, when the wellbore has just been constructed, the cement sheath undergoes hydration and volumetric shrinkage. Creep deformation is not yet significant, and the system is assumed to behave elastically (*no-creep case*). The corresponding initial stress state is evaluated analytically (1)–(3), accounting for the constant formation pressure and temperature, as well as the volumetric contraction of the cement during setting.

After a long time, the structural response approaches the steady-state creep regime described in paragraph 3.2. The governing equations formulated in terms of velocity and mean hydrostatic pressure for steady-state creep are discretized using the finite element method. This mixed formulation requires special care in the choice of interpolation spaces to ensure numerical stability under the incompressibility constraint.

The steady-state creep behavior can be described by the equations of incompressible viscous flow (11)–(13). The weak formulation is obtained by multiplying the momentum balance and incompressibility equations by the test functions $\boldsymbol{\psi}_{\dot{u}}$ and ψ_q, respectively, and integrating over the domain. Applying Gauss's theorem, we obtain the final weak form

$$\begin{aligned} &\int_V 2\eta\,\varepsilon(\dot{\mathbf{u}}) : \varepsilon(\boldsymbol{\psi}_{\dot{u}})\ \mathrm{d}V - \int_V q\ \mathrm{div}\,\boldsymbol{\psi}_{\dot{u}}\ \mathrm{d}V = \\ &\quad = -\int_{\Gamma_\infty} \boldsymbol{\psi}_{\dot{u}} \cdot \mathrm{diag}(\sigma_{\min}, \sigma_{\max}) \cdot \mathbf{n}\ \mathrm{d}s, \\ &\int_V \nabla\psi_q\ \cdot \dot{\mathbf{u}}\ \mathrm{d}V = 0, \end{aligned} \tag{17}$$

where $\boldsymbol{\psi}_{\dot{u}} \in [H^1(V)]^2$ such that $\boldsymbol{\psi}_{\dot{u}}|_{\Gamma_{\mathrm{SC}}} = 0$ and $\psi_q \in L^2(V)$ are admissible test functions.

To satisfy the Ladyzhenskaya–Babuška–Brezzi (LBB) condition, which guarantees the stability and uniqueness of the mixed velocity-pressure solution, Taylor–Hood elements are employed [30]. In this formulation, the velocity field is approximated using finite element spaces with polynomial basis functions of order $(n+1)$, while the pressure (mean stress) field is interpolated using polynomials of order n. This choice provides a stable discretization and avoids spurious pressure oscillations that may occur with equal-order elements.

Operational loading stage. After the initial stress state is obtained, the subsequent thermoporoelastic response of the system is simulated numerically.

At this stage, the finite element model solves the semi-coupled linear thermo-poroelastic equations using the previously computed initial stress field $\boldsymbol{\sigma}^0$ as the initial condition.

The weak formulation is derived by multiplying the governing equations (4), (6), and (7) by the corresponding test functions $\boldsymbol{\psi}_u$, ψ_p, and ψ_T, respectively, and integrating over the domain. For the equilibrium equation, this procedure represents the virtual work of internal and external forces. The test function for displacements, $\boldsymbol{\psi}_u$, belongs to the vector Sobolev space $[H^1(V)]^2$, while the test functions for pore pressure and temperature, ψ_p and ψ_T, belong to the scalar Sobolev space $H^1(V)$. These functions satisfy the following boundary conditions:

$$\psi_T|_{\Gamma_{\text{in}}} = 0, \quad \psi_T|_{\Gamma_\infty} = 0, \quad \psi_p|_{\Gamma_\infty} = 0, \tag{18}$$

where zero values are imposed on the boundaries with the Dirichlet conditions.

The weak form of the equilibrium equation (4), accounting for the boundary conditions (8), (9) and the initial conditions (10) for displacement and stress, is written as

$$\begin{aligned} &\int_V \boldsymbol{\sigma}^0 : \boldsymbol{\varepsilon}(\boldsymbol{\psi}_u)\,\mathrm{d}V \;+\; \int_V \big(\mathbb{C} : \boldsymbol{\varepsilon}(\mathbf{u})\big) : \boldsymbol{\varepsilon}(\boldsymbol{\psi}_u)\,\mathrm{d}V \\ &\quad - \int_V b\,(p - p^0)\;\operatorname{div}\boldsymbol{\psi}_u\,\mathrm{d}V - \int_V 3\alpha_s K\,(T - T^0)\;\operatorname{div}\boldsymbol{\psi}_u\,\mathrm{d}V \\ &\quad = \; -\int_{\Gamma_{\text{in}}} \boldsymbol{\psi}_u \cdot p_w(t)\,\mathbf{n}\,\mathrm{d}S \;- \int_{\Gamma_\infty} \boldsymbol{\psi}_u \cdot \operatorname{diag}(\sigma_{\min}, \sigma_{\max}) \cdot \mathbf{n}\,\mathrm{d}S. \end{aligned} \tag{19}$$

For an isotropic elastic material (5), the elastic contribution can be written as

$$\int_V \big(\mathbb{C} : \boldsymbol{\varepsilon}(\mathbf{u})\big) : \boldsymbol{\varepsilon}(\boldsymbol{\psi}_u)\,\mathrm{d}V = \int_V \Big[\lambda\;\operatorname{tr}\boldsymbol{\varepsilon}(\mathbf{u})\;\;\operatorname{tr}\boldsymbol{\varepsilon}(\boldsymbol{\psi}_u) + 2G\,\boldsymbol{\varepsilon}(\mathbf{u}) : \boldsymbol{\varepsilon}(\boldsymbol{\psi}_u)\Big]\mathrm{d}V. \tag{20}$$

The weak forms of the pore pressure and temperature equations (6) and (7) are obtained analogously:

$$\int_V \psi_p\, b\,\frac{\partial(\operatorname{tr}\boldsymbol{\varepsilon})}{\partial t}\;\mathrm{d}V + \int_V \psi_p \frac{1}{M}\frac{\partial p}{\partial t}\;\mathrm{d}V + \int_V \frac{k}{\mu_f}\nabla\psi_p \cdot \nabla p\;\mathrm{d}V = \int_V 3\psi_p \alpha_m \frac{\partial T}{\partial t}\;\mathrm{d}V, \tag{21}$$

$$\int_V \psi_T C_m \frac{\partial T}{\partial t}\;\mathrm{d}V + \int_V \kappa \nabla\psi_T \cdot \nabla T\;\mathrm{d}V = 0. \tag{22}$$

Time integration is performed using a Rosenbrock-type method [27], which belongs to the class of linearly implicit Runge–Kutta schemes. These methods offer strong numerical stability for stiff systems and enable efficient error estimation by combining stage solutions of varying orders of accuracy. In

particular, the implementation includes the third-order ROS3 method [28]. Adaptive time stepping is governed by a proportional-integral (PI) controller that relies on local truncation error estimates [29], ensuring both accuracy and computational efficiency over long simulation times.

5 Numerical Results

This section presents the numerical results for the representative wellbore system consisting of the casing, the cement sheath, and the surrounding formation. This analysis aims to demonstrate how the initial stress state and long-term creep behavior affect stress evolution. The resulting stress changes can significantly influence the risk of failure in the cement sheath.

5.1. Verification of the steady-state creep solution. To verify the correctness of the implemented numerical algorithm, a closed-form analytical solution for the steady-state creep of an incompressible viscous medium around a circular cavity has been derived.

The solution is obtained using the velocity stream function Ψ, an approach analogous to the stream function in incompressible fluid mechanics. The velocity components are related to the stream function via

$$\dot{u}_r(r,\theta) = \frac{1}{r}\frac{\partial \Psi}{\partial \theta}, \qquad \dot{u}_\theta(r,\theta) = -\frac{\partial \Psi}{\partial r}, \tag{23}$$

which ensures zero volumetric strain. In this formulation, the incompressibility constraint $\operatorname{tr}\dot{\boldsymbol{\varepsilon}} = 0 \quad \Leftrightarrow \quad \operatorname{div}\dot{\mathbf{u}} = 0$ is satisfied automatically by construction.

The general solution for the velocity field is expressed through the stream function

$$\Psi(r,\theta) = \left(a_1 r^4 + a_2 r^2 + a_3 + a_4 r^{-2}\right)\sin 2\theta, \tag{24}$$

which yields the radial and tangential velocity components

$$\dot{u}_r = \frac{2(a_1 r^6 + a_2 r^4 + a_3 r^2 + a_4)}{r^3}\cos 2\theta, \tag{25}$$

$$\dot{u}_\theta = -\frac{2(2a_1 r^6 + a_2 r^4 - a_4)}{r^3}\sin 2\theta. \tag{26}$$

The choice of this form is motivated by the symmetry of the cylindrical wellbore geometry and by the harmonic structure of the boundary conditions on the radial stress, which contain the $\cos 2\theta$ mode. The separation into radial and angular parts follows the same logic as in Airy's stress-function method, where suitable harmonic expansions are used to satisfy equilibrium and boundary conditions.

The stress tensor components follow the constitutive law for a Newtonian incompressible medium (13), where the following ansatz is used for the hydrostatic pressure:

$$q(r,\theta) = q_0(r) + q_1(r)\cos 2\theta, \tag{27}$$

so that the angular variation of stresses is consistent with the boundary conditions. This approach provides a convenient semi-analytical solution for the steady-state creep of an incompressible viscous medium around a circular cavity.

Substituting these expressions into the equilibrium equations (11) in cylindrical coordinates yields the radial dependence of the pressure terms:

$$q_0(r) = \alpha = \text{const}, \qquad q_1(r) = 4\eta\left(\frac{a_3}{r^2} + 3a_1 r^2\right). \tag{28}$$

The external boundary of the domain, $r = r_{\text{ext}}$, is subjected to *in-situ* far-field stresses

$$\sigma_{rr}(r_{\text{ext}}, \theta) = -P_0 + S_0 \cos 2\theta, \qquad \sigma_{r\theta}(r_{\text{ext}}, \theta) = -S_0 \sin 2\theta, \tag{29}$$

where

$$P_0 = \frac{\sigma_{\max} + \sigma_{\min}}{2}, \qquad S_0 = \frac{\sigma_{\max} - \sigma_{\min}}{2}. \tag{30}$$

At the internal boundary of the cavity, $r = r_{\text{int}}$, corresponding to the "casing–cement" interface, the velocity is assumed to vanish:

$$\dot{u}_r(r_{\text{int}}, \theta) = 0, \qquad \dot{u}_\theta(r_{\text{int}}, \theta) = 0. \tag{31}$$

Using the boundary conditions for the radial and tangential stresses and matching the coefficients of the harmonic expansion, we first obtain the constant part of the hydrostatic pressure, $\alpha = P_0$. Applying the remaining conditions yields a linear system for the coefficients a_i of the stream function. The solution of this system gives

$$\begin{aligned}
a_1 &= \frac{r_{\text{ext}}^2 r_{\text{int}}^2 S_0 \left(r_{\text{ext}}^2 - r_{\text{int}}^2\right)}{2\eta\left(r_{\text{ext}}^8 + 4r_{\text{ext}}^6 r_{\text{int}}^2 - 6r_{\text{ext}}^4 r_{\text{int}}^4 + 4r_{\text{ext}}^2 r_{\text{int}}^6 + r_{\text{int}}^8\right)},\\
a_2 &= \frac{S_0\left(r_{\text{ext}}^8 - 3r_{\text{ext}}^4 r_{\text{int}}^4 + 4r_{\text{ext}}^2 r_{\text{int}}^6\right)}{4\eta\left(r_{\text{ext}}^8 + 4r_{\text{ext}}^6 r_{\text{int}}^2 - 6r_{\text{ext}}^4 r_{\text{int}}^4 + 4r_{\text{ext}}^2 r_{\text{int}}^6 + r_{\text{int}}^8\right)},\\
a_3 &= -\frac{S_0\left(r_{\text{ext}}^8 r_{\text{int}}^2 + r_{\text{ext}}^2 r_{\text{int}}^8\right)}{2\eta\left(r_{\text{ext}}^8 + 4r_{\text{ext}}^6 r_{\text{int}}^2 - 6r_{\text{ext}}^4 r_{\text{int}}^4 + 4r_{\text{ext}}^2 r_{\text{int}}^6 + r_{\text{int}}^8\right)},\\
a_4 &= \frac{r_{\text{ext}}^4 r_{\text{int}}^4 S_0\left(r_{\text{ext}}^4 + r_{\text{int}}^4\right)}{4\eta\left(r_{\text{ext}}^8 + 4r_{\text{ext}}^6 r_{\text{int}}^2 - 6r_{\text{ext}}^4 r_{\text{int}}^4 + 4r_{\text{ext}}^2 r_{\text{int}}^6 + r_{\text{int}}^8\right)}
\end{aligned} \tag{32}$$

The components of the stress tensor are obtained as

$$\sigma_{rr}(r, \theta) = -P_0 + \frac{4\eta\left(a_2 r^4 - 2a_3 r^2 - 3a_4\right)}{r^4}\cos 2\theta, \tag{33}$$

$$\sigma_{\theta\theta}(r, \theta) = -P_0 - \frac{4\eta\left(6a_1 r^6 + a_2 r^4 - 3a_4\right)}{r^4}\cos 2\theta, \tag{34}$$

$$\sigma_{r\theta}(r, \theta) = -\frac{4\eta\left(3a_1 r^6 + a_2 r^4 + a_3 r^2 + 3a_4\right)}{r^4}\sin 2\theta, \tag{35}$$

$$q(r, \theta) = P_0 + 4\eta\left(\frac{a_3}{r^2} + 3a_1 r^2\right)\cos 2\theta \tag{36}$$

Figure 5 compares the analytical steady-state creep solution with the numerical results obtained using the finite-element model. The figures include only the cement and formation regions. For verification, we assume that the cement and formation have the same viscosity $\eta = 10^3$ GPa · s. The far-field stresses are set to $\sigma_{\min} = 20$ MPa and $\sigma_{\max} = 35$ MPa. The profiles of the radial, tangential, and shear stress components versus the radius demonstrate good agreement between the numerical and analytical solutions. This confirms the accuracy of the numerical procedure and the correctness of the applied boundary conditions.

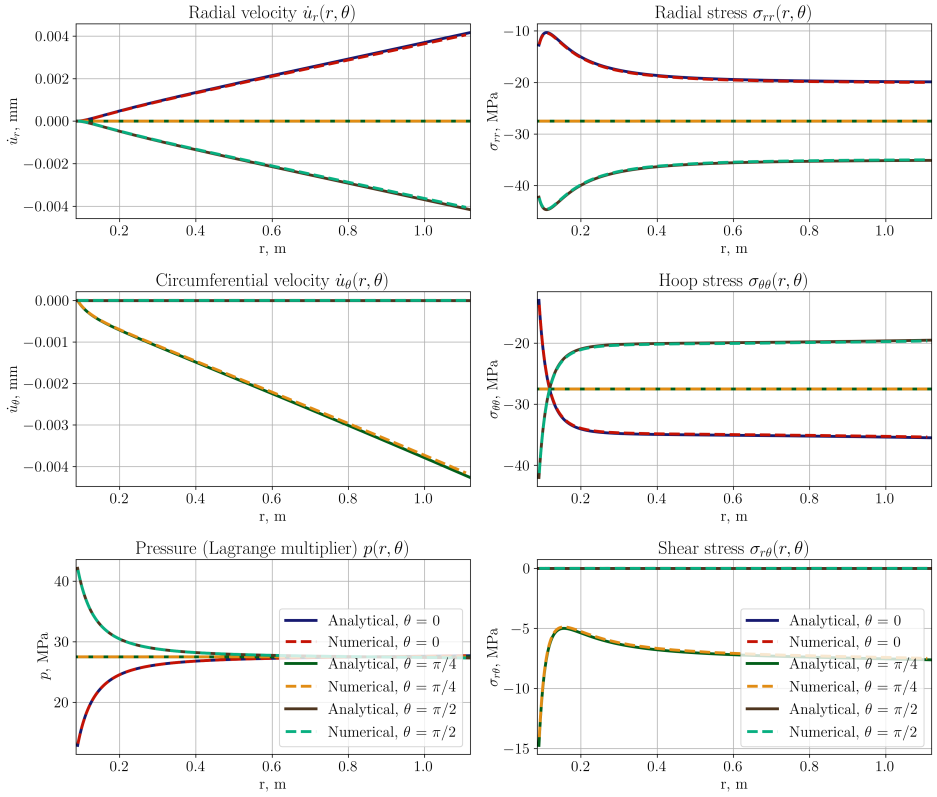

FIG. 5. Verification of the steady-state creep solution: comparison between analytical and numerical stress distributions.

5.2. Model setup. The material parameters used in the simulations are summarized in Table 1, while the geometric parameters of the wellbore and casing, as well as the pore fluid properties, are given in Table 2. The tables represent typical values for steel casing, the cement sheath, and the surrounding rock formation. The pore fluid is considered to be a weakly compressible, single-phase Newtonian fluid.

TABLE 1. Material properties used in the simulations.

Property	**Casing**	**Cement**	**Formation**
Young's modulus E [GPa]	200	12.4	15.0
Poisson's ratio ν	0.30	0.22	0.25
Skeleton density ρ [kg/m^3]	7936	2000	2280
Skeleton specific heat capacity C_p [J/(kg·K)]	500	1600	950
Thermal conductivity κ [W/(m·K)]	40	0.8	2.3
Skeleton linear thermal expansion coefficient α [10^{-6}/K]	12	10	11
Creep viscosity η [GPa·s]	–	1000	100
Porosity ϕ	–	0.2	0.2
Biot coefficient b	–	0.7	0.7
Permeability k [m^2]	–	10^{-18}	10^{-15}

TABLE 2. Well geometry and pore fluid properties.

Parameter	**Value**	**Unit**
Well construction geometry		
Wellbore diameter	0.28	m
Casing inner diameter	0.16	m
Casing outer diameter	0.18	m
Cement sheath thickness	0.05	m
Casing eccentricity offset δ	0.025	m
Eccentricity angle γ	$\pi/2$	rad
Pore fluid properties		
Density ρ_f	1000	kg/m^3
Specific heat capacity C_p	2100	J/(kg·K)
Linear thermal expansion coefficient α	70	10^{-6}/K
Bulk modulus K_f	500	MPa
Dynamic viscosity μ	0.5	mPa·s

The model incorporates anisotropic *in-situ* stresses and loading conditions. The far-field stress state is defined as

$$\sigma_{\min} = 25 \text{ MPa}, \quad \sigma_{\max} = 35 \text{ MPa}, \quad \sigma_{\mathrm{v}} = 45 \text{ MPa}. \tag{37}$$

The initial pore pressure is set to $p_0 = 25$ MPa, and the initial temperature is equal to $T_0 = 50°\mathrm{C}$.

In the no-creep case, the displacement fluid and cement slurry pressures are set to $p_{\mathrm{d}} = p_{\mathrm{c}} = 30$ MPa, and the cement volumetric shrinkage strain is

$\varepsilon_{\text{vol}} = 0.002$. For the steady-state creep case, the displacement fluid pressure is also $p_{\text{d}} = 30$ MPa.

The wellbore pressure and temperature are given in Table 3. Two thermal scenarios are analyzed: (1) constant temperature $T_w = 50°\text{C}$, and (2) cooling from 50°C to 35°C, with the temperature in both cases corresponding to supercritical CO_2.

Each of these thermal cases is combined with two loading conditions: the early-time and the steady-state creep conditions. All simulations are performed for for 10000 seconds (2 hours 47 minutes) using adaptive time-stepping based on the ROS3 scheme.

TABLE 3. Loading schedule for operational stage.

Time [s]	Pressure [MPa]	Temperature [°C]
0	20	50
1000	40	35
10000	40	35

5.3. Discussion of results. The stress analysis is performed using the Drucker–Prager failure criterion, which serves as an indicator of potential yielding or loss of mechanical integrity in the cement sheath. It is computed as

$$f_{\text{DP}} = \alpha I_1 + \sqrt{J_2} - k, \tag{38}$$

where I_1 is the first invariant of the Terzaghi effective stress tensor $\boldsymbol{\sigma}' = \boldsymbol{\sigma} - p\,\mathbf{I}$, J_2 is the second invariant of the deviatoric stress tensor, α and k are material constants defining the failure surface. Even though plasticity is not explicitly modeled, the function f_{DP} provides a convenient measure of the degree of overstress, helping to identify regions that are most susceptible to failure. The parameters α and k are defined through the uniaxial compressive and tensile strength limits σ_c, σ_t of each material as

$$\alpha = \frac{1}{\sqrt{3}} \frac{\sigma_c - \sigma_t}{\sigma_c + \sigma_t}, \qquad k = \frac{2}{\sqrt{3}} \frac{\sigma_c\, \sigma_t}{\sigma_c + \sigma_t}. \tag{39}$$

The adopted strength parameters are $\sigma_t = 10^6$ MPa, $\sigma_c = 10^6$ MPa for the steel casing such that extremely large strength parameters effectively disregard failure in the casing; $\sigma_t = 3$ MPa, $\sigma_c = 40$ MPa for the cement sheath; $\sigma_t = 3.5$ MPa, $\sigma_c = 40$ MPa for the rock formation.

The results show a marked difference between the early-time and long-term regimes (Figure 6). In the early-time case, high stress concentrations develop within the cement sheath near the casing interface, slightly extending into the formation. The maximum value of the Drucker–Prager criterion reaches 11 MPa under cooling conditions and 8.6 MPa at constant temperature, indicating stronger overstress due to thermal contraction. In contrast, for the steady-state creep regime, long-term stress relaxation leads to lower

values of the criterion: 8.1 MPa under cooling and 5.8 MPa at constant temperature. While the regions of elevated overstress remain localized near both the casing–cement and cement–formation interfaces, their magnitude is reduced, indicating that creep mitigates the risk of debonding or cracking.

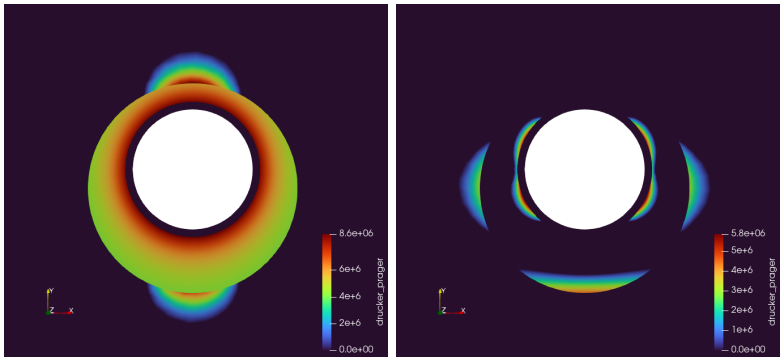

(a) Early-time, constant temperature

(b) Steady-state creep, constant temperature

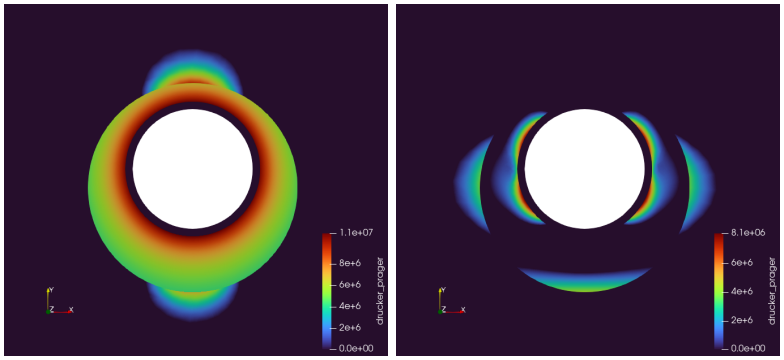

(c) Early-time, cooling

(d) Steady-state creep, cooling

FIG. 6. Spatial distribution of the Drucker–Prager overstress function at the end of the simulation.

A more detailed comparison of the radial and hoop stress components along the radius (negative y direction) is presented in Figure 7 for the constant-temperature case. The light-gray and light-brown shaded regions correspond to the cement sheath and the surrounding rock formation, respectively. The results show that stresses in the early-time regime are systematically higher than those in the long-term case. In this regime, both the radial and hoop stresses are shifted toward tension, reflecting a more pronounced stress concentration near the casing–cement interface ($r \approx 0.18$ m). These tensile stresses increase the value of the Drucker–Prager overstress function, indicating a higher risk of debonding or cracking along the cement–casing and cement–formation interfaces.

Under steady-state creep conditions, the overall stress level decreases due to long-term relaxation, while noticeable discontinuities remain at the material interfaces. The hoop stress $\sigma_{\theta\theta}$ still exhibits a pronounced peak near the inner boundary and slightly exceeds the early-time value in the outer rock region ($r \gtrsim 0.5$ m), reflecting the stress redistribution due to creep. The radial stress σ_{rr}, while following a similar trend, remains somewhat more compressive in the creep case.

This behavior illustrates the stress relaxation effect caused by long-term creep, which reduces the amplitude of stress fluctuations and promotes a more uniform and stable mechanical state within the wellbore system.

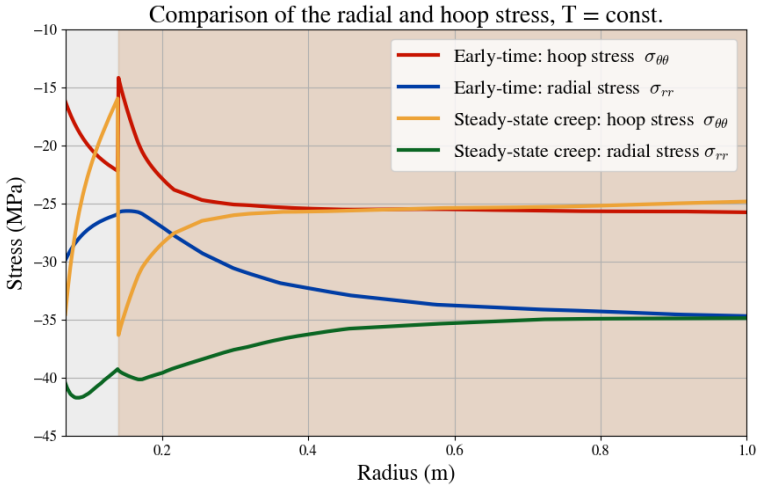

FIG. 7. Radial distribution of the stress components σ_{rr} and $\sigma_{\theta\theta}$ along the negative y direction for the constant-temperature case. The light-gray and light-brown shaded regions indicate the cement sheath and the surrounding rock formation, respectively.

6 Conclusion

This study examines stress evolution around wells using a semi-coupled thermoporoelastic framework, which accounts for multi-stage loading and the effects of cement shrinkage in the near-wellbore region.

The analysis of two scenarios, corresponding to a newly created and an late-life well, demonstrates the critical influence of the initial stress state. In the early stage, immediately after the cement sets, the cement behaves as a linear elastic solid that cannot effectively redistribute loads, resulting in high stress gradients around the casing-cement interface. Over longer time scales, creep allows the cement to gradually relax these highly stressed zones, producing a more uniform stress distribution and more effective stress transfer between the casing and the cement sheath. This stabilizing effect of

cement creep reduces stress fluctuations and mitigates the risk of interfacial degradation.

The analysis of the stress state using the Drucker-Prager failure criterion highlights the stress responses of the cement sheath and the surrounding formation in early-time and long-term regimes. In the early-time regime, the cement behaves as an elastic solid that has not yet redistributed the loads after setting. This leads to pronounced stress concentrations near the casing–cement interface and an increased risk of local debonding or cracking. In contrast, under steady-state creep, long-term stress relaxation reduces the magnitude of overstress, as indicated by a decrease in f_{DP}. Although elevated stresses remain near the interfaces, their magnitude decreases, demonstrating the stabilizing effect of creep. These results emphasize that the initial stress state, determined by the sequence of drilling, cementing, and shrinkage, has a controlling influence on near-wellbore stress distribution. Long-term creep, in turn, contributes to a more equilibrated and mechanically stable configuration. Overall, the findings provide a quantitative basis for assessing potential overstress zones and optimizing cement integrity in well design and long-term operation.

Linear elasticity provides insights into the primary stress trends. However, it is inherently limited by its inability to describe nonlinear material behavior, damage accumulation, and failure mechanisms. Despite these limitations, the framework successfully captures the key interactions governing stress evolution in the near-wellbore region. It also provides a foundation for more advanced coupled or nonlinear modeling in future work.

References

[1] H. Jo, K.E. Gray, *Mechanical behavior of concentric casing, cement, and formation using analytical and numerical methods*, in: ARMA US Rock Mechanics/Geomechanics Symposium, ARMA–10 (2010), Salt Lake City, Paper No. ARMA-10-142.

[2] M. Loizzo and others, *Quantifying the risk of CO_2 leakage through wellbores*, SPE Drilling & Completion, **26**:3 (2011), 324–331.

[3] M. Loizzo, B. Lecampion, S. Mogilevskaya, *The role of geological barriers in achieving robust well integrity*, Energy Procedia, **114** (2017), 5193–5205.

[4] M.C.M. Nasvi, P.G. Ranjith, J. Sanjayan, A. Haque, X. Li, *Mechanical behaviour of wellbore materials saturated in brine water with different salinity levels*, Energy, **66** (2014), 239–249.

[5] Y. Wang, Y. Feng, Y. Zhao, S. Li, F. Su, C. Gu, X. Li, *Experimental study on cement sheath integrity of UGS wells under cyclic loading*, Geoenergy Sci. Engineer., **239** (2024), Article No. 212958.

[6] A.V. Valov et al., *Thermoporoelastic model for the cement sheath failure in a cased and cemented wellbore*, J. Petroleum Sci. Engineer., **210** (2022), Article No. 109916.

[7] V. Vilarrasa, S. Olivella, J. Carrera, J. Rutqvist, *Long term impacts of cold CO_2 injection on the caprock integrity*, Int. J. Greenhouse Gas Control, **24** (2014), 1–13.

[8] R. Zhang, P.H. Winterfeld, X. Yin, Y. Xiong, Y.-S. Wu, *Sequentially coupled THMC model for CO_2 geological sequestration into a 2D heterogeneous saline aquifer*, J. Natural Gas Sci. Engineer., **27**:2 (2015), 579–615.

[9] T.S. Valente, A. Ventura Gouveia, J.A.O. Barros, *A new basic creep model coupled with a thermomechanical model for the numerical simulation of the time-dependent behaviour of concrete structures*, in G. Pijaudier-Cabot, P. Grassl and C. La Borderie (Eds), 10th International Conference on Fracture Mechanics of Concrete and Concrete Structures (FraMCoS-X), Bayonne, 2019.

[10] X. Su, Y. Wu, M. Jia, Z. Liu, J. Jiang, and W. Xu, *Multiscale creep model for concrete considering from C-S-H gel scale to mesoscale with ITZ and irregular-shaped aggregates*, Cement Concrete Composites, **143** (2023), Article No. 105254.

[11] H. Sone, M.D. Zoback, *Time-dependent deformation of shale gas reservoir rocks and its long-term effect on the in situ state of stress*, Int. J. Rock Mech. Mining Sci., **69** (2014), 120–132.

[12] M. Zhang, S. Bachu, *Review of integrity of existing wells in relation to CO_2 geological storage: What do we know?*, Int. J. Greenhouse Gas Control, **5**:4 (2011), 826–840.

[13] Y. Wu, H. Patel, S. Salehi, *Thermal considerations of cement integrity in geothermal wells*, in: The 45th Workshop on Geothermal Reservoir Engineering, Stanford, California, 2020, Article ID SGP-TR-216.

[14] V. Vilarrasa, A.P. Rinaldi, J. Rutqvist, *Long-term thermal effects on injectivity evolution during CO_2 storage*, Int. J. Greenhouse Gas Control, **64** (2017), 314–322.

[15] Y. Wang, *Simulating coupled THM problem and wellbore integrity analyses with two-phase fluid flow in naturally fractured reservoirs*, SPE Asia Pacific CCUS Conference, Kuala Lumpur, Malaysia, 2025, Paper ID SPE-225823-MS.

[16] M.E. Kozhevnikova, T.A. Rotanova, A.V. Valov, *Computer simulation of the plane thermoelasticity problems: comparative analysis of coupled and uncoupled statements*, Vychisl. Mekh. Splosh. Sred, **10**:4 (2017), 388–398.

[17] K. E. Gray, E. Podnos, E. Becker, *Finite-element studies of near-wellbore region during cementing operations: Part I*, SPE Drilling & Completion, **24**:1 (2009), 127–136.

[18] Y. Feng, E. Podnos, K.E. Gray, *Well integrity analysis: 3D numerical modeling of cement interface debonding*, in: ARMA US Rock Mechanics/Geomechanics Symposium, ARMA–2016, Houston, 2016, Paper No. ARMA-2016-246.

[19] E.G. Kirsch, *Die Theorie der Elastizität und die Bedürfnisse der Festigkeitslehre*, Zeitschrift des Vereines deutscher Ingenieure, **42** (1898), 797–807.

[20] M. Hazrati Aghchai, P. Moarefvand, H.Salari Rad, *On analytic solutions of elastic net displacements around a circular tunnel*, J. Mining Environment, **11**:2 (2020), 419–432.

[21] M. Meng, L.P. Frash, J.W. Carey, W. Li, N.J. Welch, W. Zhang, *Cement stress and microstructure evolution during curing in semi-rigid high-pressure environments*, Cement Concrete Research, **149** (2021), Paper No 106555.

[22] K.R. Backe, P. Skalle, O.B. Lile, *Shrinkage of oil well cement slurries*, J. Can. Pet. Technol., **37**:9 (1998), Paper No PETSOC-98-09-06.

[23] W. Zhang, A. Eckert, *Numerical investigation of the influence of cement failure to micro-annuli generation*, in 52nd US Rock Mechanics/Geomechanics Symposium, Seattle, Washington, 2018, Paper No ARMA-2018-224.

[24] M. Samudio, *Modelling of an oil well cement paste from early age to hardened state: hydration kinetics and poromechanical behaviour*, PhD Thesis, Université Paris-Est, 2017.

[25] S. Panjwani, J. McDaniel, M. Nikolaou, *Improvement of zonal isolation in horizontal shale gas wells: A data-driven model-based approach*, J. Natural Gas Sci. Engin., **47** (2017), 101–113.

[26] Z. Zhou, *Creep and stress relaxation of an incompressible viscoelastic material of the rate type*, Int. J. Solids Struct., **28**:5 (1991), 617–630. Zbl 0754.73045

[27] E. Hairer, G. Wanner, *Solving ordinary differential equations. II: Stiff and differential-algebraic problems*, Springer, Berlin, 1996. Zbl 0859.65067

[28] A. Sandu et al., *Benchmarking stiff ODE solvers for atmospheric chemistry problems II: Rosenbrock solvers*, Atmospheric Environment, **31**:20 (1997), 3459–3472.
[29] G. Söderlind, *Automatic control and adaptive time-stepping*, Numer. Algorithms, **31**:1-4 (2002), 281–310. Zbl 1012.65080
[30] D. Boffi, F. Brezzi, M. Fortin, *Mixed finite element methods and applications*, Springer, Berlin, 2013. Zbl 1277.65092
[31] W. Bangerth, R. Hartmann, G. Kanschat, *deal.II — a general-purpose object-oriented finite element library*, ACM Trans. Math. Softw., **33**:4 (2007), Article No 24. Zbl 1365.65248
[32] S. Timoshenko, J. Goodier, *Theory of elasticity*, McGraw-Hill, New York etc., 1970. Zbl 0266.73008

Ksenia Sergeevna Sukhinina
Novosibirsk State University,
st. Pirogova, 1,
630090, Novosibirsk, Russia
Email address: k.sukhinina@g.nsu.ru

Alexander Viktorovich Valov
Novosibirsk State University,
st. Pirogova, 1,
630090, Novosibirsk, Russia,
Lavrentyev Institute of Hydrodynamics SB RAS,
630090, Novosibirsk, Russia
Email address: a.valov@g.nsu.ru

Aleksey Valeryevich Shutov
Novosibirsk State University,
st. Pirogova, 1,
630090, Novosibirsk, Russia,
Lavrentyev Institute of Hydrodynamics SB RAS,
630090, Novosibirsk, Russia
Email address: a.shutov@g.nsu.ru